DOI: https://doi.org/10.2138/am-2018-6425

Revision 1

Electronic properties and compressional behavior of Fe–Si alloys at high pressure

Seiji Kamada[1,2,*], Nanami Suzuki[2], Fumiya Maeda[2], Naohisa Hirao[3], Maki Hamada[2,4], Eiji Ohtani[2], Ryo Masuda[5], Takaya Mitsui[6], Yasuo Ohishi[3], Satoshi Nakano[7]

1: Frontier Research Institute for Interdisciplinary Sciences, Tohoku University, Sendai, 980-8578, Japan.
2: Department of Earth Science, Tohoku University, Sendai, 980-8578, Japan.
3: Japan Synchrotron Radiation Research Institute, Sayo, Hyogo, 679-5198, Japan.
4: School of Natural System, College of Science and Engineering, Kanazawa University, Kanazawa, 920-1192, Japan.
5: Research Reactor Institute, Kyoto University, Osaka, 590-0494, Japan.
6: National Institute for Quantum and Radiological Science and Technology, Sayo, Hyogo, 679-5148, Japan.
7: National Institute for Materials Science, Tsukuba, 305-0044, Japan.
*: Corresponding author.

Abstract

Planetary cores are composed mainly of Fe with minor elements such as Ni, Si, O, and S. The physical properties of Fe alloys depend on their composition. Changes in *c*/*a* ratio, center shifts, and elastic properties of Fe and Fe–Ni alloys were reported previously. However, such properties of Fe–light–element alloys have not yet been extensively studied. Si is a plausible candidate as a light element in

planetary cores. Therefore, we studied the electronic properties and compressional behavior of Fe-Si alloys with a hexagonal-close-packed (hcp) structure under high pressure using synchrotron Mössbauer spectroscopy (SMS) and X-ray diffraction (XRD). Center shifts (CS) were observed at pressures of 21.4–45.3 GPa for Fe–2.8wt.%Si and of 30.9–62.2 GPa for Fe–6.1wt%.Si. Some of SMS and XRD measurements were performed under the same conditions using a newly developed system at the BL10XU beamline of SPring-8, which allowed simultaneous characterization of the electron information and crystal structure. Changes in the CS values were observed at 36.9 GPa in Fe–2.8wt%.Si and 54.3 GPa in Fe–6.1wt%.Si. The ratios of *c*/*a* in the hcp structure were measured at pressures of 21.2–49.6 GPa in Fe–2.8wt.%Si and 32.9–61.4 GPa in Fe–6.1wt.%Si. The *c*/*a* ratio changed at pressures of 30–45 GPa in Fe–2.8wt.%Si and at 50 GPa in Fe–6.1wt.%Si. Changes in the CS and *c*/*a* ratio were explained according to the electronic isostructural transition in Fe–Si alloys. In addition, the transition pressure increased with increasing Si content in metallic iron. This finding is significant as changes in seismic wave velocities due to the change in *c*/*a* ratio of Fe–Si alloys with an hcp structure might be observed if Venus has a solid inner core.

Keywords: Synchrotron Mössbauer spectroscopy; diamond anvil cell; electronic topological transition; compressional behavior; Fe-Si alloy

Introduction

Iron is one of the main constituents of Earth and other terrestrial planets, and hence, is an element of interest in planetary studies. The Earth's core is divided into an outer liquid core and an inner solid core based on seismological observations. These cores are less dense than pure metallic iron under the high pressure and temperature conditions corresponding to the core conditions. This density deficit of the cores suggests a presence of one or more light elements in addition to Fe. Silicon has been proposed as a viable candidate for one of the light elements in the core as it is one of the most abundant elements on Earth (Birch 1952; Ringwood 1959).

Iron is stable in a hexagonal-close-packed (hcp) structure up to the conditions of the Earth's core. The physical properties of hcp Fe have been studied at conditions of high pressure and temperature (e.g., Anzellini et al. 2013; Dewaele et al. 2006; Fiquet et al. 2001; Mao et al. 1990; Ohtani et al. 2013; Sakai et al. 2014; Sakamaki et al. 2016; Tateno et al. 2010). According to previous studies, the densities and seismic wave velocities of the Earth's inner core could not be explained if the core was pure Fe. Therefore, it is important to investigate the effects of light elements on the physical properties of Fe. Phase relationships in Fe–Si systems have been investigated at high pressures and temperatures, showing that hcp structures of Fe–Si alloys were stable under the core conditions (e.g., Fischer et al., 2012; 2013; Lin et al., 2002; 2009; Tateno et al., 2015). The compressional behavior (e.g., Fischer et al. 2012; 2013; Hirao et al. 2004; Tateno et al. 2015) and sound velocities of hcp Fe–Si alloys (e.g., Badro et al. 2007; Lin et al. 2003b; Mao et al. 2012) have been measured at high pressure and temperature in order to evaluate the contribution of Si to the density deficit and seismic velocity in the inner core. Lin et al. (2003a) and Hirao et al. (2004) estimated the amount of Si in the Earth's inner core to be in the range of 3–5 wt.% based on studies on the compressional behavior. According to compressional behavior and sound velocity studies, Badro et al. (2007) concluded that the Earth's inner core contained 2.3 wt.% of Si. Antonangeli et al. (2010) investigated sound velocities of Fe–Ni–Si alloys and proposed that the amount of Si in the core is 1–2 wt.% with 4–5 wt.% Ni.

Recently, Glazyrin et al. (2013) reported that hcp Fe and hcp Fe–Ni alloys experienced an electronic topological transition (ETT; Lifshitz 1960), which was not accompanied by a structural transition, based on X-ray diffraction (XRD), Mössbauer spectroscopy, sound velocity measurements, and theoretical calculations. They observed changes in the evolution of the *c/a* ratio with increasing pressure and a drastic increase in the Mössbauer center shift (CS) at around 40 GPa. They measured Debye sound velocities of Fe and Fe–Ni alloys and observed a change in the pressure effect at around 40 GPa. They reported a change in $\mathrm{d}V_{\mathrm{Debye}}/\mathrm{d}P$ before and after the ETT of hcp Fe and Fe–Ni alloys. The slope of the curve ($\mathrm{d}V_{\mathrm{Debye}}/\mathrm{d}P$) below 40 GPa was larger than that above 40 GPa, suggesting that the sound velocities after the ETT occurred were lower than estimated sound velocities based on sound velocities before the ETT occurred. These results clearly show that the contribution of the EET in Fe alloys should be considered when discussing the sound velocities and/or structures in solid planetary cores.

The ETT should also be studied at high temperature for various Fe alloys (e.g., Fe–Si, Fe–Ni–Si, Fe–S) in order to consider any possible effects on the core. Since a change in the pressure dependency of the *c*/*a* ratio is related to the ETT, as shown by Glazyrin et al. (2013), it is also important to consider this relationship at high temperature. Ono et al. (2010) reported a change in the pressure dependency of the *c/a* ratio of hcp Fe at room temperature at around 50 GPa, while Ono (2015) reported that a similar change in hcp Fe occurred at 2000 K at around 150 GPa. Thus, there is possibility that the ETT and change in *c/a* may occur in the Earth and planetary cores. Although the ETT in Fe and Fe–Ni alloys was investigated at high pressure and temperature, the electronic properties and *c/a* ratios have not yet been investigated in Fe–light-element alloys under hydrostatic conditions. Since Si is a prime candidate for a light element in the core and substitutes Fe in the same was as Ni, we examined the structural, electronic, and compression properties of Fe–Si alloys with hcp structure up to 60 GPa using a combination of XRD and synchrotron-based Mössbauer spectroscopy (SMS). We used the data to estimate the effect of Si on the ETT and *c/a* evolution as a function of pressure the interior of terrestrial cores.

Experimental procedure

The starting materials for the Fe–Si alloys were synthesized from pellets of powder mixtures of Fe and Si, which was 33% enriched in ^{57}Fe. The pellets were melted using a double-sided laser heating system with a reducing atmosphere of 99 at.% Ar and 1 at.% H_2 to avoid oxidation of the samples. The molten samples were quenched to room temperature by shutting off the laser power after heating for 5 seconds with a laser power between 20 and 30 W. These samples were polished and their chemical compositions were analyzed by a field-emission scanning electron microscope (FE-SEM, JEOL JSM-7001F) with energy dispersive X-ray spectroscopy (EDS), which confirmed compositions of Fe–2.8wt.%Si (5 at.% Si) and Fe–6.1wt.%Si (12 at.% Si). A homogeneous texture was also observed under FE-SEM. Chips from the polished samples with a thickness of 15 μm were used for energy-domain SMS and in situ XRD experiments at high pressure conditions.

A symmetric diamond anvil cell (DAC) with a culet size of 300 or 450 μm (depending on the desired pressure) was used to generate high pressure. A pre-indented rhenium gasket with a thickness of 40 μm was drilled to produce a sample chamber with a diameter of half of the culet size used. After placing the starting material and some ruby chips into the sample chamber, helium gas was loaded into the chamber as a pressure medium using a gas-loading system described previously (Takemura et al. 2001).

Room-temperature XRD patterns were collected at the BL10XU beamline of SPring-8 (Ohishi et al. 2008). Typical X-ray wavelengths were 0.4134(1) or 0.4425(1) Å and pinhole collimators with a diameter of 20 or 50 μm were used. An imaging plate (IP; Rigaku R-AXIS IV^{++}, 300 × 300 mm^2, 0.10 mm pixel size) or a flat panel detector (XRD0822, Perkin Elmer, Inc.) was used as an X-ray detector. X-ray diffraction images were converted into conventional one-dimensional X-ray profiles by IPAnalyzer software package, where the 1D profiles were analyzed using the PDIndexer software package (Seto et al. 2010).

The energy domain SMS measurements using a nuclear Bragg monochromator were performed at the BL10XU and BL11XU beamlines at SPring-8 (Mitsui et al. 2009). The X-ray energy used in the SMS experiments was set to 14.4125 keV using double monochromatic crystals, while the bandwidth of the incident X-rays was set to ~3 meV using a high-resolution monochromator (HRM). The HRM was placed in front of the sample when using the BL11XU beamline or behind the sample when using the BL10XU beamline in order to record the XRD patterns. The 14.4 keV single-line ^{57}Fe Mössbauer radiation from the broadband synchrotron radiation was filtered using an electronically forbidden pure nuclear Bragg reflection (333) of a $^{57}FeBO_3$ single crystal near the Néel temperature in an external magnetic field. The final energy bandwidth of the X-ray beam was around 15 neV. The Mössbauer resonance energy of the $^{57}FeBO_3$ crystal was controlled using the Doppler effect of light by oscillating the crystal, which was mounted on a velocity transducer and operated in a sinusoidal-acceleration mode, parallel to the reflection plane. The ^{57}Fe Mössbauer radiation was counted using a NaI scintillation detector. A typical data collection time for one spectrum was 2 hours. Mössbauer spectra were referenced to a standard metallic iron foil at 1 atm and room temperature in air. The MossA software package (Prescher et al. 2012) was used for computational analysis and the spectra were fitted using a Lorentzian model.

The experimental pressure was measured using a ruby florescence method (Dewaele et al. 2008). The experimental pressure was determined as the average of pressures before and after the SMS or XRD measurements. The unceartainty in the pressure was considered to be the standard deviation of the measured pressures. Since helium was used as a pressure medium, the pressure distribution or differences between the values before and after the measurements were ≤ 0.4 GPa. Therefore, the stress effect on the center shift and *c/a* ratio was suppressed.

Results and discussion

Mössbauer spectra and XRD patterns from the hcp phases of Fe–2.8wt.%Si and Fe–6.1wt.%Si were obtained up to 60 GPa at room temperature. The hyperfine structure and unit cell parameters are summarized in Tables 1 and 2, respectively. A typical SMS spectrum is shown in Fig. 1, where a single peak from Fe–2.8wt%Si or Fe–6.1wt%Si at all pressures was observed, suggesting they were nonmagnetic within the present experimental resolution. The relationships between the CS and pressures for the present Fe–Si alloys are shown in Fig. 2, together with those of pure iron and the $Fe_{0.9}Ni_{0.1}$ alloy by Glazyrin et al. (2013). The CS of Fe–2.8wt.%Si was decreased with increasing pressure up to 35 GPa, were constant around -0.49 mm/sec in the range of 36 to 42 GPa, then decreased again above 43 GPa. The CS of Fe–6.1wt.%Si decreased up to 54 GPa. When the sample was pressurized at 57 GPa, the CS increased drastically from -0.286 mm/sec to -0.02 mm/sec. Similar changes in CS were observed by Glazyrin et al. (2013) for pure iron and the $Fe_{0.9}Ni_{0.1}$ alloy; they observed an increase in CS at ~40 GPa and concluded that the ETT occurred at this pressure based on a DFT calculation. The difference in CS before and after the ETT in Fe was much smaller than that in $Fe_{0.9}Ni_{0.1}$. In this study, we also observed similar behaviors in Fe–Si alloys. The large change in CS values was not observed for Fe–2.8wt.%Si, whereas the CS for Fe–6.1wt.%Si was 0.284 mm/sec and similar behavior was observed in Glazyrin et al. (2013), which was a large CS change in $Fe_{0.9}Ni_{0.1}$ compared to that of Fe. According to Glazyrin et al (2013), if this transition is the ETT, this shift is due to the change of second order Doppler shift as a result of the change of the topology of Fe electronic states, and *c*/*a* ratio should also show anomaly. Here, we observed that adding Si to Fe increased the pressure of the CS change from 40 to 54 GPa in this study. Assuming Si randomly substitutes Fe, as the Si content increases, the average number of Si atoms that occur as a nearest neighbor atom in the hcp crystal structure increases. Since Si has less electrons than Fe, the electron density at a Fe nucleus in the hcp structure of Fe–Si alloys is smaller than that of Fe in the hcp structure of Fe. Thus, a higher pressure is required to achieve the ETT with increasing Si content.

XRD patterns of Fe–2.8wt.%Si and Fe–6.1wt.%Si were recorded under a pressure of 11 to 61 GPa. Only hcp structured phases in Fe–2.8wt.%Si and Fe–6.1wt.%Si were observed above 21 GPa and 29 GPa, respectively. The 100, 002,

This is a preprint, the final version is subject to change, of the American Mineralogist (MSA)
Cite as Authors (Year) Title. American Mineralogist, in press.
DOI: https://doi.org/10.2138/am-2018-6425

101, 102, 110, and 103 reflections were observed up to the highest pressure. The *c/a* ratios were obtained for hcp structures and their pressure dependencies are shown in Fig. 3. The *c/a* ratios of hcp Fe-Si alloys coexisting with bcc Fe-Si alloys are not shown in Fig. 3 due to the scattered data (probably due to the influence of the bcc phase). Although the error bars for the *c/a* ratios are large, the *c/a* ratio of Fe–2.8wt.%Si had a consistent value of 1.610 up to 30 GPa, decreased slightly to 1.606 at 45 GPa, and remained constant above this pressure. On the other hand, the *c/a* ratio for Fe–6.1wt.%Si slightly decreased up to 50 GPa, at which point it suddenly increased up to 1.613, decreased to 1.611 at around 51 GPa, and then stayed constant under further compression. Ono et al. (2010) observed that the *c/a* ratio of hcp-Fe decreased up to 50 GPa and then stayed nearly constant above 50 GPa. A similar anomalous behavior as observed in Fe was also observed in Fe–Si alloys. The pressure where anomalous behavior occurred increased with increasing Si contents in Fe. Since we used helium gas as a pressure medium in the SMS and XRD measurements, changes in CS and *c/a* (as shown in Figs. 2 and 3, respectively) are not due to the pressure distribution. Therefore, the changes may have been due to the ETT.

The equation of states (EOS) for Fe–Si alloys were also obtained in this study. P–V data set were fitted to the 3rd order Birch-Murnaghan EOS (3BM; eq. 1) and Vinet EOS (VEOS; eq. 2).

$$P = \frac{3}{2}K_0\left(\left(\frac{V_0}{V}\right)^{\frac{7}{3}} - \left(\frac{V_0}{V}\right)^{\frac{5}{3}}\right)\left[1 - \frac{3}{4}(4 - K')\left(\left(\frac{V_0}{V}\right)^{\frac{2}{3}} - 1\right)\right], \qquad (1)$$

$$P = 3K_0\left(\frac{V}{V_0}\right)^{\frac{-2}{3}}\left[1 - \left(\frac{V}{V_0}\right)^{\frac{1}{3}}\right]\exp\left\{\frac{3}{2}(K'-1)\times\left[1 - \left(\frac{V}{V_0}\right)^{\frac{1}{3}}\right]\right\}, \qquad (2)$$

where P and V are the experimental pressure in GPa and the experimental volume in Å^3, V_0 is the volume at zero pressure in Å^3, K_0 is the bulk modulus at zero pressure in GPa, and K' is the pressure derivative of the bulk modulus. V_0 values for Fe–2.8wt.%Si and Fe–6.1wt.%Si were obtained based on a g–G plot (Jeanloz 1981), which is used for a material that is stable only under high pressure in order to estimate its V_0 value. G and g represent a normalized pressure and an effective strain and they are expressed as $G=P/\{3(1+2g)^{5/2}\}$ and $g=1/2\times\{(V_2/V_{01})^{-2/3}-1\}$, respectively, where V_2 represents the volume of a high pressure phase and V_{01} is a reference volume of a low pressure phase at a reference pressure. The g–G plots for hcp Fe–2.8wt.%Si and hcp Fe–6.1wt.%Si are shown in Fig. 4(a). Here, V_{01} was set as 23.44(2) Å^3 for bcc Fe-2.8wt%Si at ambient pressure for hcp Fe–2.8wt.%Si and 21.89(6) Å^3 for bcc Fe–6.1wt.%Si at 11.5 GPa. The average values of V_0 from the 2nd and 3rd g–G plots were used as V_0 for hcp Fe–2.8wt.%Si and hcp Fe–6.1wt.%Si, respectively. K_0 and K' were obtained from fitting using the constant V_0. The V_0 values from g–G plots were used for the VEOS fits as a reference (e.g., Mao et al. 1990). Although we observed anomalous behavior in the *c/a* ratio, we did not see any change in the *P–V* plots, as shown in Fig. 4(b). The volumes of hcp Fe–Si alloys coexisting with a bcc phase were also used for EOS fitting as the volumes did not show any anomalies.

Following this procedure, we fitted 3BM and VEOS to the data over the explored conditions, where the obtained parameters are listed in Table 3 along with those reported in previous studies for comparison. V_0 was also treated as a free parameter during the fits and obtained V_0, K_0, and K' values are also listed in Table 3. The present V_0 values obtained from g–G plots are consistent with V_0 obtained as the free parameter during the fits in this study. Obtained K_0 and K' values for a fixed V_0

DOI: https://doi.org/10.2138/am-2018-6425

were also consistent (within uncertainties) to those obtained with the free V_0 values. The compression curves with fixed V_0 are shown in Fig. 4(b). The black and gray solid curves represent 3BM for Fe–2.8wt.%Si and Fe–6.1wt.%Si, respectively. The black and gray dashed curves are VEOS for Fe–2.8wt.%Si and Fe–6.1wt.%Si, respectively. The K_0 values for Fe–2.8wt.%Si were found to be 196 GPa for 3BM and 195 GPa for VEOS. Those of Fe–6.1wt.%Si were 187 GPa for both 3BM and VEOS. These obtained values are similar to those reported by Asanuma et al. (2011) and Hirao et al. (2004), while larger than those reported by Lin et al. (2003) and Tateno et al. (2015), although these differences can be attributed to the different V_0 values. As shown in Table 3, we recalculated V_0 of Asanuma et al. (2011) and Tateno et al. (2015) based on g–G plots, where it is clear that the obtained V_0 values were consistent with our values within error bars. The small K_0 reported by Lin et al. (2003) and Fischer et al. (2014) can be explained by their large V_0 values (which result in small K_0). The hcp Fe–6.1wt.%Si has a larger unit cell volume than that of hcp Fe–2.8wt.%Si below 40 GPa, while above 40 GPa, these volumes are similary. This suggests that Si in Fe slightly increases the unit cell volumes at relatively low pressures, as reported by Fischer et al. (2014).

Implication for Planetary cores

We fitted the c/a data using a Bolztmann sigmoidal function, as follows (Boehler et al. 2008):

$$c/a = (c/a)_f + \frac{(c/a)_i - (c/a)_f}{1 + \exp\left(\frac{P - P_{tr}}{dx}\right)}, \qquad (3)$$

where $(c/a)_f$ and $(c/a)_i$ are final and initial c/a ratio values, respectively, P is the pressure in GPa and P_{tr} is the pressure at the inflection point of the eq. (3) in GPa, and dx is related to the slope at P=P_{tr}. Eq. (3) was fitted to the experimental data, which yielded P_{tr} values of 37.7(1.8) and 39.8(1.9) for Fe–2.8wt.%Si and Fe–6.1wt.%Si, respectively, with $(c/a)_f$ and $(c/a)_i$ values of 1.6054(3) and 1.6105(2) for Fe–2.8wt.%Si and 1.6108(8) and 1.6128(2) for Fe–6.1wt.%Si, which were obtained by averaging the initial and final data in Fig. 3. A similar fitting was performed for Fe data by Glazyrin et al. (2013), where $(c/a)_f$ and $(c/a)_i$ showed a proportional relationship to pressure, yielding P_{tr}=34.1(4.2). If P_{tr} is considered as the transition pressure where changes in the c/a ratio occur, the pressure increased with increasing Si content in the Fe–Si alloy. The relationship between the transition pressure P_{tr} and Si content can be expressed as follows if a linear relationship is assumed:

$$P_{tr} = 0.196(92) \times C_{\mathrm{Si\ in\ Fe}} + 34.4(7), \quad (4)$$

where $C_{\mathrm{Si\ in\ Fe}}$ is the Si content in Fe [at%]. As reported by Ono (2015), P_{tr} may increase with increasing temperature. If the gradient of temperature–pressure relationship in Ono (2015) is applicable to the Fe–Si alloys, the effect of Si addition on P_{tr} under high temperature can be estimated. The estimated transition pressure–temperature relationships are shown in Fig. 5 along with Mercury, Venus, Earth, and Mars core conditions and Fe phase relationship. The transition P–T relationships for pure Fe, Fe–6wt.%Si, and Fe–10wt.%Si were obtained using P_{tr} at room temperature and the temperature gradient from Ono (2015). The temperature profiles for Mercury and Mars are based on data from Rivoldini et al. (2009) and Rivoldini et al. (2011), respectively, while the core conditions for Venus are from Aitta (2012) and Lodders and Fegley (1998). Although we do not know exactly whether the terrestrial planets have solid inner cores due to lack of seismological data, our results indicate that only Venus's core could undergo a change in c/a ratio, as shown in Fig. 5. For Mercury and Mars, the core conditions are too hot compared to the transition *P*–*T*. It should be noted that the Fe–alloys in the Mercury and Mars cores have an fcc structure rather than an hcp structure. Therefore, the transition probably does not occur under the conditions relevant for the cores of Mercury and Mars. On the other hand, the core temperature of the Earth is lower than the transition temperature. Therefore, a change in the c/a ratio might not be observed. In Venus, the temperature profile of the core intersects the transition conditions. The intersect pressures are between 237 and 251 GPa for the hot-core model and 173 and 187 GPa for the cold-core model, which corresponds to solid inner cores with radii of approximately 1300 and 2300 km, respectively. If Venus has a solid inner core and the inner core intercept boundary of the c/a changes as shown in Fig. 5, the inner core may have slower seismic wave velocities compared to those estimated under lower pressure conditions than an ETT pressure (e.g., Glazyrin et al. 2013). However, changes in the c/a ratios of Fe–Si alloys were not investigated in the previous and this study under such high temperatures and pressures, and this point should be clarified in a future study. The present results show that the change in c/a becomes unclear as increasing Si contents; it might be dificult to detect such changes in c/a in Fe–Si alloys for high Si contents.

Acknowledgments

S.K. was supported by a Grant-in-Aid for Young Scientists (B) (No. 25800291) and E.O. was supported by a Grant-in-Aid for Scientific Research from the Ministry of Education, Culture, Science, Sport, and Technology of the Japanese Government (Nos. 22000002 and 15H05748). The synchrotron radiation experiments were performed at the SPring-8 facility with the approval of the Japan Synchrotron Radiation Research Institute

(Proposal Nos. 2013A1496, 2013A3513, 2013B0104, 2013A3517, 2014A0104, 2014A1910, 2014A3516, 2014B0104, 2014A3519, 2015A0104, and 2015B0104) and Japan Atomic Energy Agency (Proposal Nos. 2013A-E01, 2013B-E07, 2014A-E06, and 2014B-E09).

References

Aitta, A. (2012) Venus's internal structure, temperature and core composition. Icarus, 218, 967–974.

Antonangeli, D., Siebert, J., Badro, J., Farber, D.L., Fiquet, G., Morard, G., and Ryerson, F.J. (2010) Composition of the Earth's inner core from high-pressure sound velocity measurements in Fe-Ni-Si alloys. Earth and Planetary Science Letters, 295, 292–296.

Anzellini, S., Dewaele, A., Mezouar, M., Loubeyre, P., and Morard, G. (2013) Melting of iron at Earth's inner core boundary based on fast X-ray diffraction. Science, 340, 464–466.

Asanuma, H., Ohtani, E., Sakai, T., Terasaki, H., Kamada, S., Hirao, N., and Ohishi, Y. (2011) Static compression of $Fe_{0.83}Ni_{0.09}Si_{0.08}$ alloy to 374 GPa and $Fe_{0.93}Si_{0.07}$ alloy to 252 GPa: Implications for the Earth's inner core. Earth and Planetary Science Letters, 310, 113–118.

Badro, J., Fiquet, G., Guyot, F., Gregoryanz, E., Occelli, F., Antonangeli, D., and d'Astuto, M. (2007) Effect of light elements on the sound velocities in solid iron: Implications for the composition of Earth's core. Earth and Planetary Science Letters, 254, 233–238.

DOI: https://doi.org/10.2138/am-2018-6425

Birch, F. (1952) Elasticity and constitution of the Earth's interior, Journal of Geophysical Research, 57, 227–286.

Birch, F. (1964) Density and composition of mantle and core, Journal of Geophysical Research, 69(20), 4377–4388.

Birch, F. (1978) Finite strain isotherm and velocities for single-crystal and polycystalline NaCl at high pressures and 300 K. Journal of Geophysical Research, 83(B), 127–1268.

Boehler, R., Santamaria-Perez, D., Errandonea, D., and Mezouar, M. (2008) Melting, density, and anisotropy of iron at core conditions: new X-ray measurements to 150 GPa. Journal of Physics: Conference Series, 121, 022018.

Dewaele, A., Belonoshko, A. B., Garbarino, G., Occelli, F., Bouvier, P., Hanfland, M., and Mezouar, M. (2012) High-pressure-high-temperature equation of state of KCl and KBr. Physical Review B, 85, 214105.

Dewaele, A., Loubeyre, P., Occelli, F., Mezouar, M., and Torrent, M. (2006) Quasihydrostatic equation of state of iron above 2 Mbar. Physical Review Letters, 97, 215504.

Dewaele, A., Torrent, M., Loubeyre, P., and Mezouar, M. (2008) Compression curves of transition metals in the Mbar range: Experiments and projector augmented-wave calculations. Physical Review B, 78, 104102.

Fischer, R.A., Campbell, A.J., Caracas, R., Reaman, D.M., Dera, P., and Prakapenka, V.B. (2012) Equation of state and phase diagram of Fe-16Si alloy as a candidate component of Earth's core. Earth and Planetary Science Letters, 357–358, 268–276.

Fischer, R.A., Campbell, A.J., Reaman, D.M., Miller, N.A., Heinz, D.L., Dera, P., and Prakapenka, V.B. (2013) Phase relations in the Fe-FeSi system at high pressures and temperatures. Earth and Planetary Science Letters, 373, 54–64.

Fischer, R.A., Campbell, A.J., Caracas, R., Reaman, N.A., Heinz, D.L., Dera, P., and Prakapenka, V.B. (2014) Equations of state in the Fe-FeSi system at high pressures and temperatures. Journal of Geophysical Research, 119, 2810–2827.

Fiquet, G., Badro, J., Guyot, F., Requardt, H., and Krisch, M. (2001) Sound velocities in iron to 110 gigapascals. Science, 291, 468–471.

Glazyrin, K., Pourovskii, L. V., Dubrovinsky, L., Narygina, O., McCammon, C., Hewener, B., Schünemann, V., Wolny, J., Muffler, K., Chumakov, A. I., Crichton, W., Hanfland, M., Prakapenka, V.B., Tasnádi, F., Ekholm, M., Aichhorn, M., Vildosola, V., Ruban, A. V., Katsnelson, M. I., and Abrikosov, I. A., (2013) Importance of correlation effects in hcp iron revealed by a pressure-induced electronic topological transition. Physical Review Letters, 110, 117206.

Hirao, N., Ohtani, E., Kondo, T., and Kikegawa, T. (2004) Equation of state of iron-silicon alloys to megabar pressure. Physics Chemistry Minerals, 31, 329–336.

Jeanloz, R. (1981) Finite-strain equation of state for high-pressure phases. Geophysical Research Letters, 8(12), 1219–1222.

Kamada, S., Ohtani, E., Terasaki, H., Sakai, T., Miyahara, M., Ohishi, Y., and Hirao, N. (2012) Melting relationships in the Fe–Fe_3S system up to the outer core conditions. Earth and Planetary Science Letters, 359–360, 23–33.

Lifshitz, I.M. (1960) Anomalies of electron characteristics of a metal in the high pressure region. Soviet Physics JETP, 11(5), 1130–1135.

DOI: https://doi.org/10.2138/am-2018-6425

Lin, J.-F., Heinz, D. L., Campbell, A.J., Devine, J.M., and Shen, G. (2002) Iron-silicon alloy in Earth's core? Science, 295, 313–315.

Lin, J.-F., Campbell, A.J., and Heinz, D. L. (2003a) Static compression of iron-silicon alloys: Implications for silicon in the Earth's core. Journal of Geophysical Research, 108(B1), 2045.

Lin, J.-F., Struzhkin, V.V., Sturhahn, W., Huang, E., Zhao, J., Hu, M.Y., Alp, E.E., Mao, H.-K., Boctor, N., and Hemley, R.J. (2003b) Sound velocities of iron-nickel and iron-silicon alloys at high pressures. Geophysical Research Letters, 30(21), 2112.

Lin, J.-F., Scott, H.P., Fischer, R.A., Chang, Y.-Y., Kantor, I., and Prakapenka, V.B. (2009) Phase relations of Fe-Si alloy in the Earth's core. Geophysical Research Letters, 36, L06306.

Lodders, K., and Fegley, Jr., B. (1998) The planetary scientist's companion. 371 p. Oxford University Press, New York.

Mao, H.K., Wu, Y., Chen, L. C., Shu, J. F., and Jephcoat, A. P. (1990) Static compression of iron to 300 GPa and $Fe_{0.8}Ni_{0.2}$ alloy to 260 GPa: Implications for composition of the core. Journal of Geophysical Research, 95(B13), 21737–21742.

Mao, Z., Lin, J.-F., Liu, J., Alatas, A., Gao, L., Zhao, J., and Mao, H.-K. (2012) Sound velocities of Fe and Fe-Si alloy in the Earth's core. Proceedings National Academy of Science, 109, 10239–10244.

Mitsui, T., Hirao, N., Ohishi, Y., Masuda, R., Nakamura, Y., Enoki, H., Sakai, K., and Seto, M. (2009) Development of an energy-domain ^{57}Fe-Mössbauer spectrometer using synchrotron radiation and its application to ultrahigh-pressure studies with a diamond anvil cell, Journal of Synchrotron Radiation, 16, 723–729.

DOI: https://doi.org/10.2138/am-2018-6425

Ohishi, Y., Hirao, N., Sata, N., Hirose, K., and Takata, M. (2008) Highly intense monochromatic X-ray diffraction facility for high-pressure research at SPring-8. High Pressure Research, 28(3), 163–173.

Ohtani, E., Shibazaki, Y., Sakai, T., Mibe, K., Fukui, H., Kamada, S., Sakamaki, T., Seto, Y., Tsutsui, S., and Baron, A.Q.R. (2013) Sound velocity of hexagonal close-packed iron up to core pressures. Geophysical Research Letters, 40, 5089–5094.

Ono, S., Kikegawa, T., Hirao, N., and Mibe, K. (2010) High-pressure magnetic transition in hcp-Fe. American Mineralogist, 95, 880–883.

Ono, S. (2015) Relationship between structural variation and spin transition of iron under high pressures and high temperatures. Solid State Communications, 203, 1–4.

Ringwood, A.E. (1959) On the chemical evolution and densities of the planets. Geochimica et Cosmochimica Acta, 15, 257–283.

Rivoldini, A., Van Hoolst, T., and Verhoeven, O. (2009) The interior structure of Mercury and its core sulfur content. Icarus, 201, 12–30.

Rivoldini, A., Van Hoolst, T., Verhoeven, O., Mocquet, A., and Dehant, V. (2011) Geodesy constraints on the interior structure and composition of Mars. Icarus, 213, 451–472.

Sakai, T., Takahashi, S., Nishitani, N., Mashino, I., Ohtani, E., and Hirao, N. (2014) Equation of state of pure iron and $Fe_{0.9}$,$Ni_{0.1}$ alloy up to 3 Mbar. Physics of Earth and Planetary Interiors, 228, 114–126.

Sakamaki, T., Ohtani, E., Fukui, H., Kamada, S., Takahashi, S., Sakairi, T., Takahata, A., Sakai, T., Tsutsui, S., Ishikawa, D., Shiraishi, R., Seto, Y., Tsuchiya, T., and Baron, A.Q.R. (2016) Constraints on Earth's inner core composition inferred from measurements of the sound velocity of hcp-iron in extreme conditions. Science Advances, 2, e1500802.

Seto, Y., Hamane, D., Nagai, T., and Sata, N. (2010). Development of a software suite on X-ray diffraction experiments. The Review of high pressure science and technology, 20(3), 269–276 (in Japanese).

Stixrude, L., Cohen, R.E., and Singh, D.J. (1994) Iron at high pressure: Linearized-augmented-plane-wave computations in the generalized-gradient approximation. Physics Review B, 50(9), 6642–6445.

Tateno, S., Hirose, K., Ohishi, Y., and Tatsumi, Y. (2010) The structure of iron in Earth's inner core. Science, 330, 359–361.

Tateno, S., Kuwayama, Y., Hirose, K., and Ohishi, Y. (2015) The structure of Fe-Si alloy in Earth's inner core. Earth and Planetary Science Letters, 418, 11–19.

Takemura, K., Sahu, P.Ch., and Toma, Y. (2001) Versatile gas-loading system for diamond-anvil cells. Review of Scientific Instruments, 72, 3873–3876.

Uchida, T., Wang, Y., Rivers, M.L., Sutton, S.R. (2001) Stability field and thermal equation of state of ε-iron determined by synchrotron X-ray diffraction in a multianvil apparatus. Journal of Geophysical Research, 106(B10), 21799–21810.

Williams, Q., Jeanloz, R., Bass, J., Svendsen, B., and Ahrens, T.J. (1987) The melting curve of iron to 250 gigapascals: a constraint on temperature at Earth's core. Science, 236, 181–182.

Yamazaki, D., Ito, E., Yoshino, T., Yoneda, A., Guo, X., Zhang, B., Sun, W., Shimojuku, A., Tsujino, N., Kunimoto, T., Higo, Y., Funakoshi, K. (2012) P-V-T equation of ε-iron up to 80 GPa and 1900 K using the Kawai-type high pressure apparatus equipped with sintered diamond anvils. Geophysical Research Letters, 39, L20308.

Figure captions

Figure 1. A typical high-pressure synchrotron Mössbauer spectrum from Fe–2.8wt.%Si at 21.4 GPa.

Figure 2. CS values as a function of pressure. The open circles and squares represent CS values for Fe–2.8wt.%Si and Fe–6.1wt.%Si measured in this study. The cross and plus symbols are data for pure iron and $Fe_{0.9}Ni_{0.1}$, respectively, from Glazyrin et al. (2013).

Figure 3. The *c/a* ratios for the metals studied here compared to those from previous studies. The triangles and inverted triangles are the present results for Fe–2.8wt.%Si and Fe–6.1wt.%Si, respectively. The present P–V data are plotted for conditions where a single hcp phase was observed. The open circles and diamonds are previous data for Fe from Glazyrin et al. (2013) and Dewaele et al. (2006), respectively.

Figure 4. (a) g–G plots of Fe–Si alloys. The P–V data coexisting with bcc Fe–Si alloys were plotted and used to obtain V_0. The black symbols show data for Fe–2.8wt.%Si, while the dark gray symbols show data for Fe–6.1wt.%Si. The black and dark gray solid lines are 2nd order g–G plots, and the dashed curves are 3rd order g–G plots. (b) Compressional behavior of Fe–2.8wt.%Si and Fe–6.1wt.%Si plotted with data from previous studies. The black triangles and dark gray inverted triangles show the volumes of Fe–2.8wt.%Si and Fe–6.1wt.%Si samples, respectively. The P–V data coexisting with bcc Fe–Si alloys are also plotted. The black solid and dashed curves show compression curves from the 3rd order Birch-Murnaghan equation of state and the Vinet

equation of state for Fe–2.8wt.%Si and dark gray solid and dashed curves show those for Fe–6.1wt.%Si.

Figure 5. Fe phase diagram with terrestrial planet core conditions and the transition boundary of *c*/*a* changes boundary based on this study and those of Glazyrin et al. (2013) and Ono et al. (2015). The Mercury and Mars core temperature and pressure conditions are based on Rivoldini et al. (2009) and Rivoldini et al. (2011), respectively. The Venus core conditions are from Aitta (2012) and Lodders and Fegley (1998). The Earth inner core conditions are based on Fe melting temperatures and studies of the effects of light element on the melting temperatures (e.g. Anzellini et al. 2013; Kamada et al. 2012).

This is a preprint, the final version is subject to change, of the American Mineralogist (MSA)
Cite as Authors (Year) Title. American Mineralogist, in press.
DOI: https://doi.org/10.2138/am-2018-6425

Tables

Table 1. Hyperfine parameters of the samples based on SMS measurements.

P [GPa]	**CS [mm/s]**	**P [GPa]**	**CS [mm/s]**
Run 1	**Fe–2.8wt.%Si**	**Run 2**	**Fe–6.1wt.%Si**
21.4(1)	-0.295(19)	30.9(4)	-0.061(62)
23.4(2)	-0.320(22)	35.9(3)	-0.066(68)
25.3(3)	-0.334(24)	39.3(1)	-0.184(44)
27.7(4)	-0.354(24)	41.3(3)	-0.167(42)
29.5(4)	-0.376(26)	43.3(1)	-0.199(40)
31.3(4)	-0.413(28)	45.8(2)	-0.237(44)
33.7(4)	-0.441(29)	49.5(1)	-0.261(51)
35.6(3)	-0.454(27)	51.4(3)	-0.278(58)
36.9(3)	-0.487(35)	52.5(2)	-0.304(50)
39.4(6)	-0.492(27)	54.3(4)	-0.286(59)
41.2(3)	-0.488(40)	57.0(3)	-0.02(16)
43.3(4)	-0.525(36)	59.4(1)	-0.194(91)
45.3(3)	-0.545(38)	62.20(3)	-0.12(13)

The numbers in parentheses show experimental uncertainties.

Pressure errors were obtained from multiple measurements of ruby chips in the chamber using Dewaele's ruby scale (Dewaele et al. 2008).

Table 2. Lattice parameters of Fe–2.8wt.%Si and Fe–6.1wt.%Si alloys at high pressure.

P [GPa]	*a* [Å]	*c* [Å]	*V* [Å^3]	*c/a*	P [GPa]	*a* [Å]	*c* [Å]	*V* [Å^3]	*c/a*
Run 3		**Fe–2.8wt.%Si hcp**			20.46(42)[a]	2.4425(3)	3.9394(7)	20.35(2)	1.6129(3)
18.95(4)[a]	2.4466(10)	3.9421(22)	20.44(5)	1.6113(11)	22.39(41)[a]	2.4356(7)	3.9342(15)	20.21(4)	1.6153(8)
20.38(20)[a]	2.4422(9)	3.9337(19)	20.32(5)	1.6107(10)	25.06(62)[a]	2.4296(5)	3.9198(13)	20.04(3)	1.6134(6)
21.15(9)	2.4398(8)	3.9292(16)	20.26(5)	1.6105(8)	27.05(48)[a]	2.4249(5)	3.9129(11)	19.92(3)	1.6137(6)
22.40(16)	2.4360(8)	3.9223(16)	20.16(5)	1.6101(8)	28.90(39)	2.4200(7)	3.9029(15)	19.79(4)	1.6128(8)
23.77(27)	2.4321(9)	3.9168(19)	20.06(5)	1.6104(10)	30.90(54)	2.4155(5)	3.8963(11)	19.69(3)	1.6130(5)
25.10(23)	2.4286(10)	3.9111(22)	19.98(6)	1.6105(11)	32.89(35)	2.4106(4)	3.8872(10)	19.56(3)	1.6125(5)
26.33(21)	2.4256(11)	3.9068(23)	19.91(6)	1.6107(12)	34.45(30)	2.4058(5)	3.8802(10)	19.45(3)	1.6128(5)
27.93(26)	2.4215(13)	3.9004(28)	19.81(8)	1.6107(14)	37.79(89)	2.3967(6)	3.8632(14)	19.22(4)	1.6119(7)
29.58(26)	2.4174(13)	3.8924(27)	19.70(8)	1.6102(14)	39.69(27)	2.3944(5)	3.8594(12)	19.16(3)	1.6118(6)
31.52(23)	2.4128(13)	3.8842(26)	19.58(7)	1.6098(14)	42.22(34)	2.3881(6)	3.8480(15)	19.01(4)	1.6113(7)
33.02(21)	2.4097(13)	3.8782(26)	19.50(7)	1.6094(14)	44.34(29)	2.3833(6)	3.8410(15)	18.90(4)	1.6116(7)
35.05(34)	2.4047(14)	3.8690(29)	19.38(8)	1.6089(15)	46.53(37)	2.3792(6)	3.8330(13)	18.79(3)	1.6111(7)
37.28(21)	2.3999(12)	3.8588(25)	19.25(7)	1.6079(13)	48.92(18)	2.3739(7)	3.8232(16)	18.66(4)	1.6105(8)
39.15(20)	2.3964(14)	3.8523(29)	19.16(8)	1.6076(15)	51.10(27)	2.3657(6)	3.8158(15)	18.49(4)	1.6130(7)
41.28(19)	2.3916(15)	3.8432(32)	19.04(9)	1.6069(17)	53.08(32)	2.3644(5)	3.8089(12)	18.44(3)	1.6109(6)
42.99(13)	2.3889(15)	3.8375(30)	18.97(8)	1.6064(16)	55.35(28)	2.3596(5)	3.8011(11)	18.33(3)	1.6109(6)
45.33(24)	2.3842(16)	3.8278(34)	18.84(9)	1.6055(18)	57.07(32)	2.3563(4)	3.7954(10)	18.25(3)	1.6107(5)
47.29(25)	2.3794(17)	3.8205(35)	18.73(9)	1.6057(18)	59.41 (41)	2.3512(3)	3.7886(8)	18.14(2)	1.6114(4)
49.61(28)	2.3756(18)	3.8131(37)	18.64(10)	1.6051(19)	61.37(28)	2.3475(5)	3.7814(13)	18.05(3)	1.6108(7)
					59.74(1)	2.3506(5)	3.7864(11)	18.12(3)	1.6108(6)
Run 4		**Fe–6.1wt%Si hcp**			58.29(3)	2.3539(6)	3.7905(14)	18.19(4)	1.6103(7)
11.44(3)[a]	2.4759(32)	3.9944(75)	21.21(20)	1.6133(37)	55.06(6)	2.3607(7)	3.8010(17)	18.34(4)	1.6101(9)
11.49(4)[a]	2.4734(28)	3.9867(65)	21.12(18)	1.6118(32)	52.22(4)	2.3678(8)	3.8112(17)	18.50(5)	1.6096(9)
12.85(10)[a]	2.4721(26)	3.9892(61)	21.11(17)	1.6137(30)	46.84(143)	2.3787(17)	3.8278(33)	18.76(4)	1.6104(8)
14.75(9)[a]	2.4639(24)	3.9816(56)	20.93(15)	1.6160(27)	42.40(39)	2.3921(16)	3.8499(30)	19.05(4)	1.6114(8)
16.93(15)[a]	2.4570(22)	3.9615(51)	20.71(14)	1.6123(25)	38.79(23)	2.3979(7)	3.8654(16)	19.25(4)	1.6120(8)
19.02(15)[a]	2.4466(23)	3.9682(54)	20.57(14)	1.6219(27)	35.05(53)	2.4076(8)	3.8797(18)	19.48(5)	1.6114(9)

The numbers in parentheses show errors. Pressure errors were obtained from multiple measurements of ruby chips in the chamber using Dewaele's ruby scale (Dewaele et al. 2008).
a: hcp Fe–Si alloys coexisted with bcc Fe-Si alloys.

DOI: https://doi.org/10.2138/am-2018-6425

Table 3. The equation of state parameters for Fe-Si alloys.

Composition	P [GPa]	V_0 [Å^3]	K_0 [GPa]	K'	EOS[a]	ref.
Fe–2.8wt.%Si	19–50	22.19(7)	186(11)	4.80(38)	3BM	This study
		22.21(7)	183(11)	5.11(40)	VEOS	
		22.13(10)[b]	196.4(10)	4.45(7)	3BM	
		22. 13 (10)[b]	195.2(11)	4.64(8)	VEOS	
Fe–6.1wt.%Si	11–61	22.35(6)	190.7(90)	3.84(27)	3BM	This study
		22.37(7)	187.9(99)	4.04(34)	VEOS	
		22.38(1)[b]	187.2(20)	3.94(11)	3BM	
		22.38(1)[b]	186.1(21)	4.10(13)	VEOS	
Fe–3.4wt.%Si	23–252	22.4(28)	196(20)	4.3(2)	3BM	Asanuma et al. (2011)
		22.28(32)[b]	203(4)	4.29(9)	3BM[c]	
Fe–7.9wt.%Si	4.5–54	22.9(1)	141(10)	5.7(6)	3BM	Lin et al. (2003)
Fe–8.7wt.%Si	23–196	22.3(8)	198(9)	4.7(3)	3BM	Hirao et al. (2004)
Fe–9.0wt.%Si	47–197	23.9(2)	129.1(14)	5.29(8)	3BM	Fischer et al. (2014)
		24.19(8)	111.4(12)	6.08(8)	VEOS	
Fe–9.0wt.%Si	13–305	22.7(2)	168(12)	5.5(2)	VEOS	Tateno et al. (2015)
		22.24(32)[b]	206(4)	5.03(9)	VEOS[d]	
Fe	35–301	22.35(3)	164.8(36)	5.33(9)	3BM	Mao et al. (1990)
		22.35(3)	160.2(21)	5.82(8)	VEOS	
	6–15	22.7(3)	135(19)	6.0(4)	3BM	Uchida et al. (2001)
	18–205	22.468(24)	165(fixed)	4.97(4)	3BM	Dewaele et al. (2006)
		22.428(98)	163.4(79)	5.38(16)	VEOS	
		22.07(30)[b]	192.8(15)	4.93(5)	VEOS[d]	
	20–83	22.15(5)	202(7)	4.5(2)	3BM	Yamazaki et al. (2012)
		22.17(6)	196(8)	4.8(2)	VEOS	
	24–279	22.16(19)[b]	184.2(22)	4.78(12)	3BM	Sakai et al. (2014)
		22.16(19)[b]	179.2(22)	5.24(12)	VEOS	
		22.07(20)[b]	195.1(2.4)	4.93(12)	3BM	
		22.07(20)[b]	189.9(2.4)	5.39(13)	VEOS	

a: 3BM and VEOS represent the 3rd order Birch-Murnaghan and Vinet EOS, respectively.

b: V_0 was fixed to the values obtained from g–G plots.

c: EOS parameters re-calculated with a fixed V_0 from a g–G plot and pressures based on NaCl B2.

d: EOS parameters re-calculated with a fixed V_0 from a g–G plot.

Figures

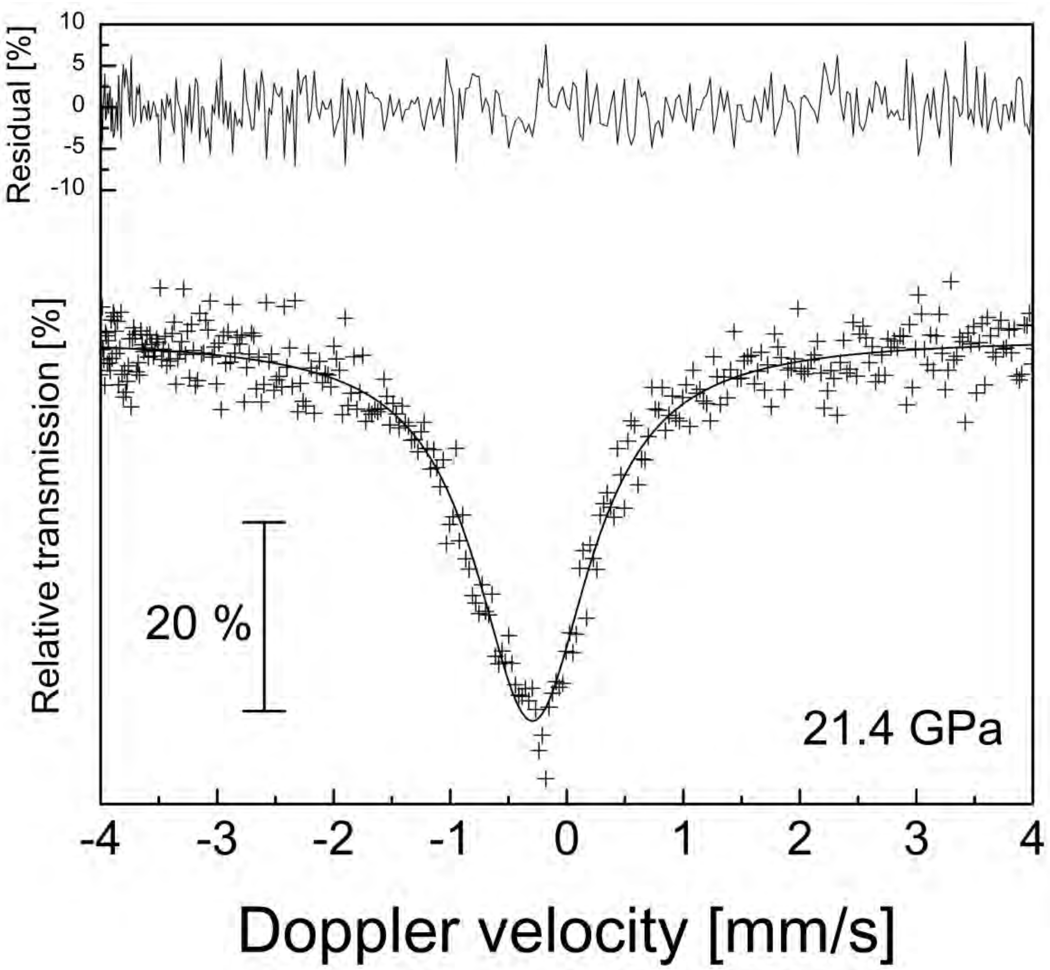

Fig. 1

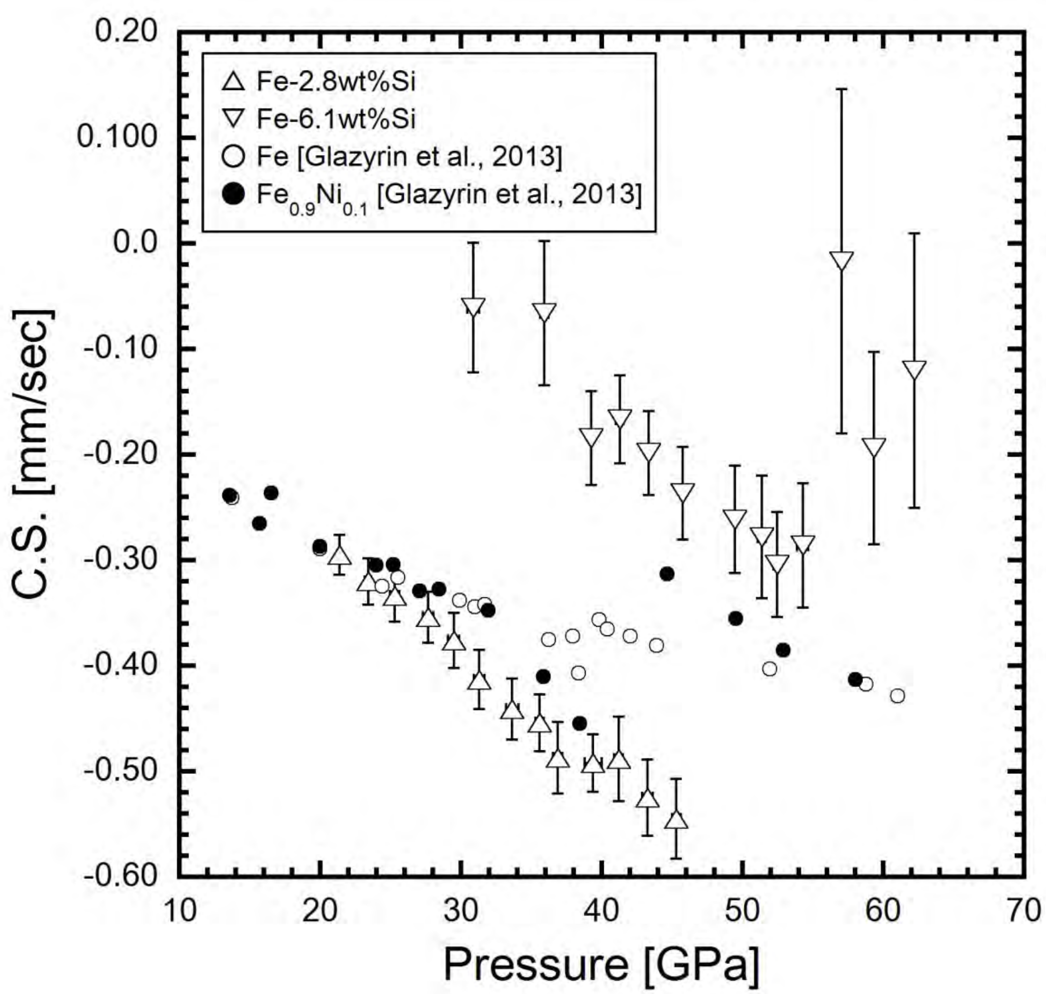
Fe-2.8wt%Si
Fe-6.1wt%Si
Fe [Glazyrin et al., 2013]
Fe0.9Ni0.1 [Glazyrin et al., 2013]
C.S. [mm/sec]
Pressure [GPa]
0.20
0.100
0.0
-0.10
-0.20
-0.30
-0.40
-0.50
-0.60
10
20
30
40
50
60
70

Fig. 2

This is a preprint, the final version is subject to change, of the American Mineralogist (MSA)
Cite as Authors (Year) Title. American Mineralogist, in press.
DOI: https://doi.org/10.2138/am-2018-6425

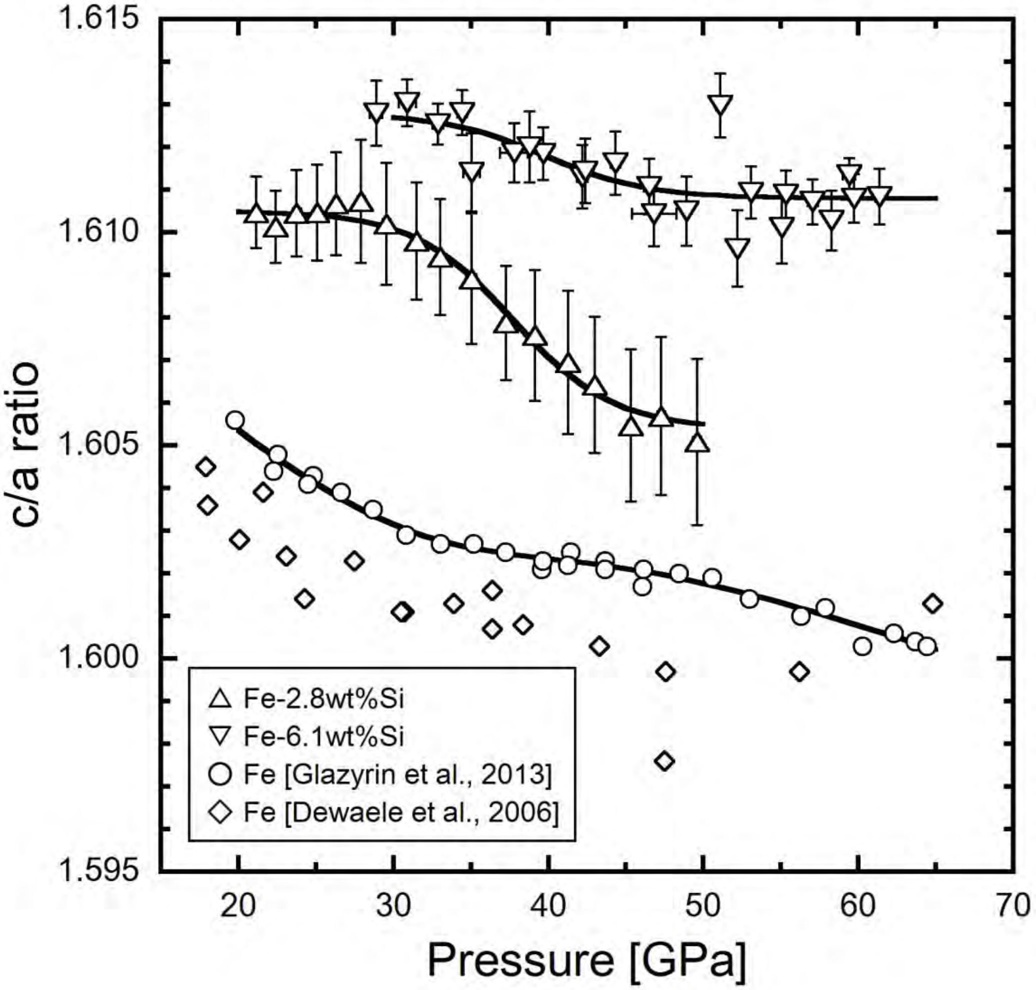

Fig. 3

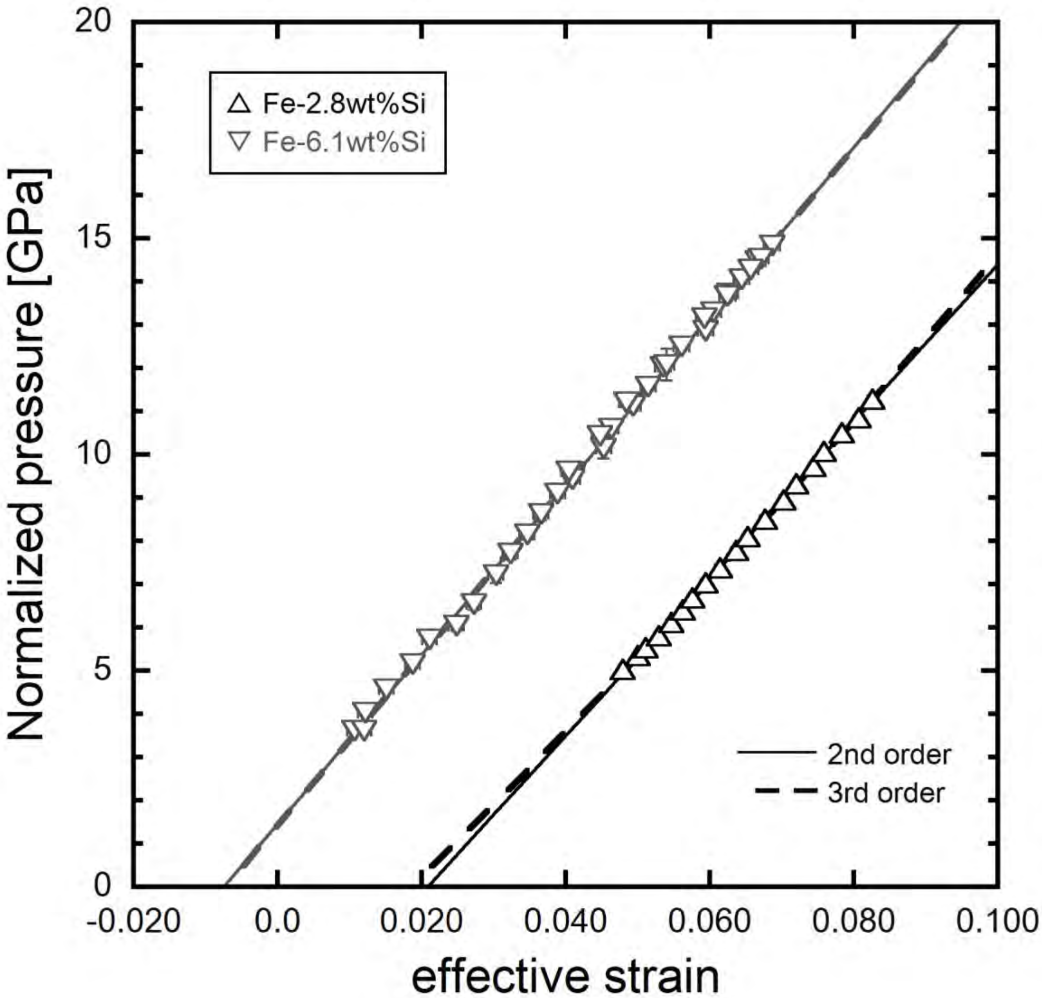
Normalized pressure [GPa]
effective strain
Fe-2.8wt%Si
Fe-6.1wt%Si
2nd order
3rd order
0
5
10
15
20
-0.020
0.0
0.020
0.040
0.060
0.080
0.100

Fig. 4(a)

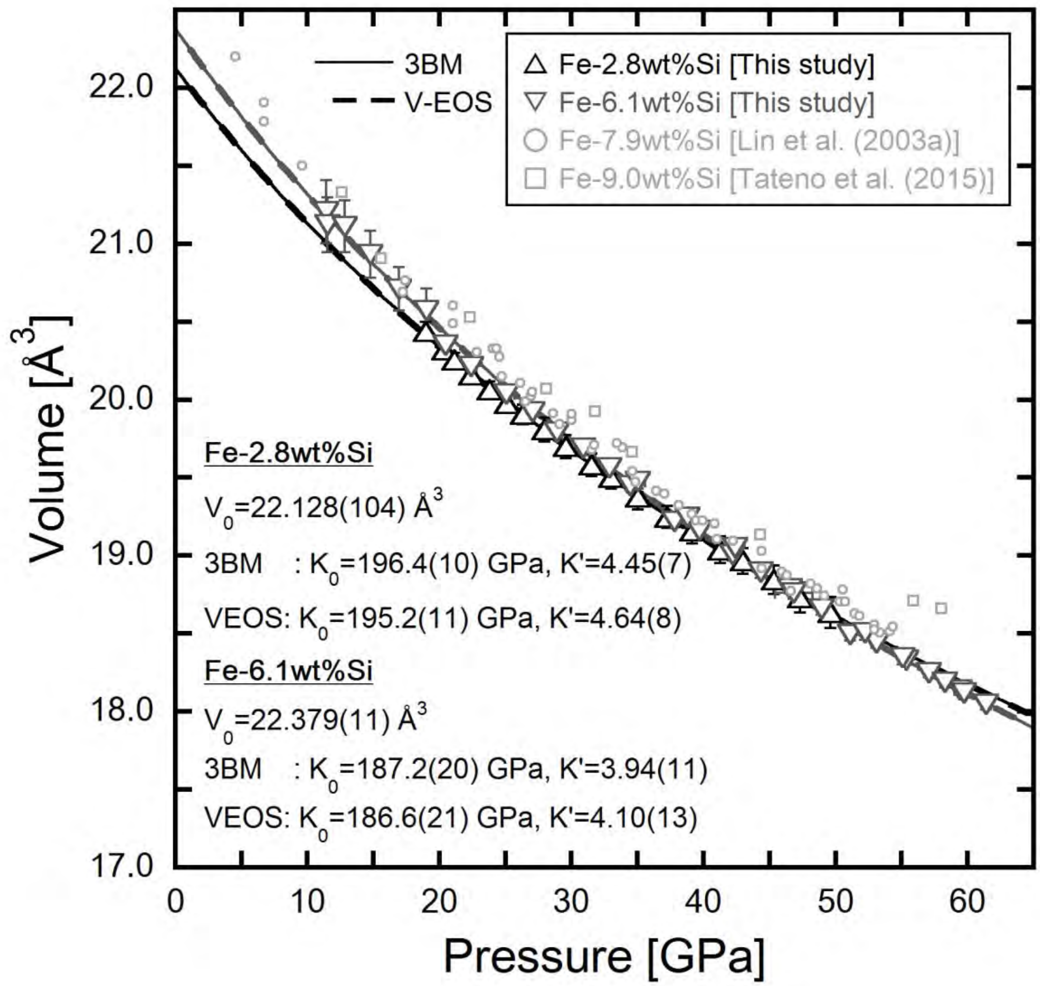
3BM
V-EOS
Fe-2.8wt%Si [This study]
Fe-6.1wt%Si [This study]
Fe-7.9wt%Si [Lin et al. (2003a)]
Fe-9.0wt%Si [Tateno et al. (2015)]
Fe-2.8wt%Si
V0=22.128(104) Å3
3BM : K0=196.4(10) GPa, K'=4.45(7)
VEOS: K0=195.2(11) GPa, K'=4.64(8)
Fe-6.1wt%Si
V0=22.379(11) Å3
3BM : K0=187.2(20) GPa, K'=3.94(11)
VEOS: K0=186.6(21) GPa, K'=4.10(13)
Volume [Å3]
Pressure [GPa]
22.0
21.0
20.0
19.0
18.0
17.0
0
10
20
30
40
50
60

Fig. 4(b)

This is a preprint, the final version is subject to change, of the American Mineralogist (MSA)
Cite as Authors (Year) Title. American Mineralogist, in press.
DOI: https://doi.org/10.2138/am-2018-6425

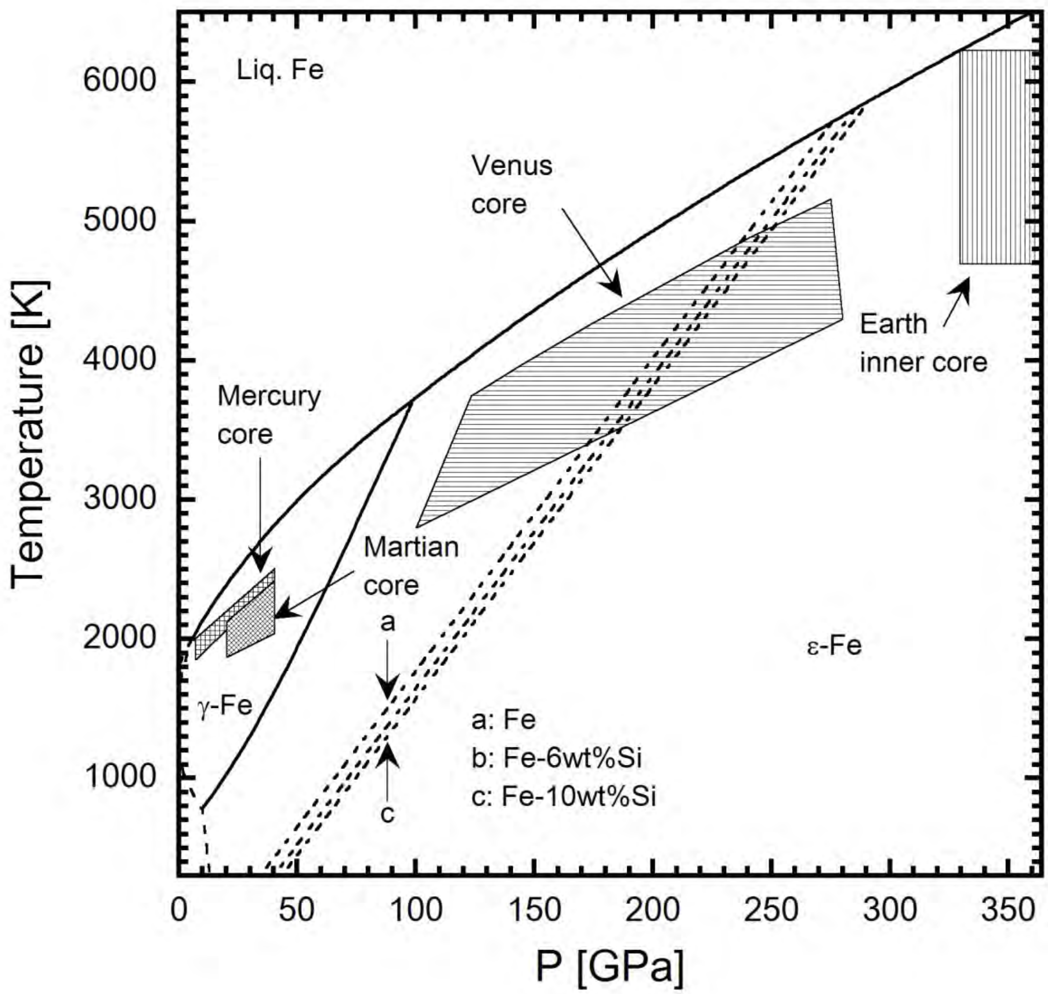

Fig. 5